ADVANCED ELECTRONIC MATERIALS Open Access
www.advelectronicmat.de

Effect of Substrate on Spin-Wave Propagation Properties in Ferrimagnetic Thulium Iron Garnet Thin Films

*Rupak Timalsina, Bharat Giri, Haohan Wang, Adam Erickson, Suchit Sarin, Suvechhya Lamichhane, Sy-Hwang Liou, Jeffrey E. Shield, Xiaoshan Xu, and Abdelghani Laraoui**

Rare-earth iron garnets have distinctive spin-wave (SW) properties such as low magnetic damping and long SW coherence length making them ideal candidates for magnonics. Among them, thulium iron garnet (TmIG) is a ferrimagnetic insulator with unique magnetic properties including perpendicular magnetic anisotropy (PMA) and topological hall effect at room temperature when grown down to a few nanometers, extending its application to magnon spintronics. Here, the SW propagation properties of TmIG films (thickness of 7–34 nm) grown on GGG and sGGG substrates are studied at room temperature. Magnetic measurements show in-plane magnetic anisotropy for TmIG films grown on GGG and out-of-plane magnetic anisotropy for films grown on sGGG substrates with PMA. SW electrical transmission spectroscopy measurements on TmIG/GGG films unveil magnetostatic surface spin waves (MSSWs) propagating up to 80 µm with a SW group velocity of 2–8 km s^{-1}. Intriguingly, these MSSWs exhibit nonreciprocal propagation, opening new applications in SW functional devices. TmIG films grown on sGGG substrates exhibit forward volume spin waves with a reciprocal propagation behavior up to 32 µm.

1. Introduction

Spin waves (or magnons) are collective dynamic magnetic excitations found in magnetically ordered materials.[1] They can be generated by injecting current,[2–4] microwave,[5,6] heating up the magnetic material,[7] or with ultrashort laser pulses.[8–10] Some of the key properties of spin waves include long coherence length (up to a few millimeters),[11] high group velocity,[12] high frequencies (up to terahertz),[10,13] and their short wavelength (down to tens of nanometers).[14,15] Other interesting properties of spin waves include nonreciprocal effect,[16] nonlinear effects,[17–19] and multiplexing,[20] making them ideal for low-energy magnetic logical operations and microwave devices.[1] Spin waves in yttrium iron garnet (YIG) have been studied extensively due to its unique magnetic properties including ultralow magnetic damping ($<10^{-4}$),[13] long spin-wave coherence length,[5,6,11] and nonlinear magnetic properties.[17–19] Moreover, there is a growing preference for magnetic materials with perpendicular magnetic anisotropy (PMA) due to their ability to efficiently excite electrically spin waves of the material with low current densities,[21–23] relevant to magnon spintronics.[13]

Thulium iron garnet ($Tm_3Fe_5O_{12}$, TmIG), a ferrimagnetic insulator with PMA,[24] has attracted an increasing interest recently for spintronics applications. It can be grown down to a few nanometers[25] while maintaining a low damping.[26] TmIG possesses Dzyaloshinskii–Moriya interaction (DMI) at room temperature[27,28] that can be increased when interfaced with heavy metals (e.g., Pt), leading to topological Hall effect at and above room temperature, which is an indication of the presence of topological spin textures such as skyrmions.[29,30] Studies of spin-wave (SW) propagation properties of TmIG films grown on different substrates are of particular interest for applications in magnon spintronics.[13] Recently, SW electrical measurements of magnetostatic forward volume spin waves (FVSWs) were reported on pristine[31] and bismuth-doped[32] TmIG films with SW velocities and decay lengths of 0.15–4.9 km s^{-1} and ≈3.2–20 µm, respectively. Nitrogen-vacancy (NV) based magnetometry measurements of magnetostatic surface spin waves (MSSWs) were performed on 34-nm-thick TmIG grown on GGG, showing a long SW decay length ≈50 µm and SW wavelength in the range of 0.8–2 µm.[33] However, no correlative measurements were reported

R. Timalsina, A. Erickson, S. Sarin, J. E. Shield, A. Laraoui
Department of Mechanical and Materials Engineering
University of Nebraska-Lincoln
900 N 16th Street, W342 NH, Lincoln, NE 68588, USA
E-mail: alaraoui2@unl.edu

B. Giri, H. Wang, S. Lamichhane, S.-H. Liou, X. Xu, A. Laraoui
Department of Physics and Astronomy and the Nebraska Center for Materials and Nanoscience
University of Nebraska-Lincoln
855 N 16th Street, Lincoln, NE 68588, USA

The ORCID identification number(s) for the author(s) of this article can be found under https://doi.org/10.1002/aelm.202400398

DOI: 10.1002/aelm.202400398

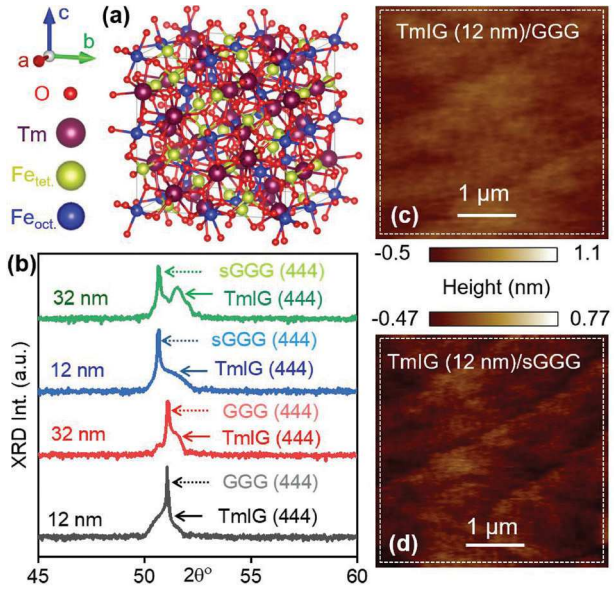

Figure 1. Characterization of TmIG films. a) A schematic of the complex unit cell of TmIG showing tetrahedral Fe (light green) and octahedral Fe (blue) lattice along Tm (purple) and O (red) atoms. b) Measured XRD spectrum of TmIG films (thickness of 12–32 nm) grown on 0.5 mm thick GGG and sGGG substrates. AFM topography image of c) TmIG (12 nm)/GGG and d) TmIG (12 nm)/sGGG films.

on the effect of substrate on the SW propagation properties of thin TmIG films.

Here, the SW transport properties of TmIG thin films (thickness of 7–34 nm) grown on GGG and sGGG substrates are studied at room temperature. Magnetic measurements by magneto-optical Kerr effect (MOKE), vibrating-sample magnetometer (VSM), and ferromagnetic resonance (FMR) spectroscopy confirm in-plane (IP) magnetic anisotropy of the TmIG films grown on GGG and out-of-plane (OOP) magnetic anisotropy for TmIG films grown on sGGG. In-plane SW electrical transmission measurements on TmIG (7–34 nm)/GGG films show MSSWs with a SW group velocity of 2–8 km s^{-1} and SW decay length of 50 μm. The MSSWs were observed to have nonreciprocal behavior, extending the application of TmIG to microwave devices (e.g., circulators).[34] Out-of-plane SW electrical transmission measurements on TmIG (32 nm)/sGGG films reveal mainly FVSWs with reciprocal behavior, propagating up to 32 μm.

2. Experimental Results and Discussion

2.1. Sample Growth and Structural Characterization

TmIG has a ferrimagnetic behavior, originating from the superexchange interactions between Tm^{+3} (Dodecahedral, Dod), Fe^{+3} (Tetrahedral, Tet), and Fe^{+3} (Octahedral, Oct) sublattices (see **Figure** 1a). A series of TmIG thin films, with a thickness of 7–34 nm (deduced from X-ray reflectometry) were grown on (111) GGG and sGGG substrates, using pulsed laser deposition.[33] Figure 1b shows X-ray diffraction (XRD) spectra for TmIG films of thicknesses 32 and 12 nm grown on GGG and sGGG substrates. For all TmIG film grown on GGG, the TmIG (444) peak is submerged within the GGG (444) peak due to the small lattice mismatch and/or the weak XRD signal obtained on thin (<15 nm) films. The lattice mismatch between TmIG and sGGG is higher, resulting in distinct XRD peaks of TmIG and sGGG. The atomic force microscopy (AFM) topography images show a smooth surface with atomic terraces and a root mean square (RMS) roughness value of about 0.3 nm for TmIG grown on both GGG (Figure 1c) and sGGG (Figure 1d), respectively, over a 4 μm × 4 μm area.

The TmIG films were also characterized using high-resolution transmission electron microscopy (HRTEM). The HRTEM image of TmIG (32 nm)/GGG film (**Figure** 2a) shows the lattice structure and reveals several dislocations with associated strain consistent with the broad XRD peaks shown in Figure 1b. Scanning TEM (STEM) was used to determine the compositional aspects of the TmIG films. The high-angle annular dark field (HAADF) image in Figure 2b shows sharp contrast between the GGG and TmIG, indicating a lack of intermixing. The layers in the lower left portion of the image are the Pt cover layers to protect the material of interest from Ga ions damage during sample preparation, accomplished via standard lift-out procedures.[35] Energy dispersive X-ray spectroscopy (EDS), in STEM mode, was used to map the elemental distributions of TmIG (32 nm)/GGG film (Figure 2c–h). The EDS maps show a clear delineation between the GGG substrate and TmIG film, with no evidence of interfacial mixing, most evident in the Fe, Tm, and Gd maps. Any Ga present in the TmIG was likely due to Ga contamination during ion milling.[35]

Elemental mapping in Figure 2b indicates no interdiffusion between different layers, similar to TmIG films grown by *off-axis* magnetron sputtering.[26] EDS microanalysis was used to determine the elemental concentrations within the sample. However, due to inherent limitations in EDS, particularly in accurately measuring low atomic number elements, it cannot be used to quantify the oxygen content. To overcome this limitation and obtain accurate elemental ratios, we used X-ray photoelectron spectroscopy (XPS) because of its higher sensitivity and energy resolution, making it well-suited for analyzing the chemical composition of materials, especially for elements like oxygen.[36,37] By employing XPS, the elemental ratios were determined, including the oxygen concentration, with greater precision. See Section S1 (Supporting Information) for details of XPS measurements on TmIG (32 nm)/GGG and TmIG (32 nm)/sGGG films. The XPS analysis[37] in Figure S1 (Supporting Information) provides valuable information about the electronic structure and oxidation states of Tm and Fe within the examined material. Linewidth of the Tm, Fe, and O in TmIG/GGG are present in 1.80, 1.10, and 2.22 eV, respectively, which are very close to the desired TmIG stoichiometry, while Tm, Fe, and O in TmIG/sGGG are present in 2.20, 1.20, and 2.50 eV, respectively. The theoretical ratio between the area of octahedral and tetrahedral Fe peaks is 2:3,[38] which is close to the measured ratios of 0.70 and 0.73 for GGG and sGGG, respectively.

2.2. Magnetic Properties of TmIG Films

The magnetic anisotropy for all TmIG films grown on GGG and sGGG substrates was investigated by MOKE spectroscopy.

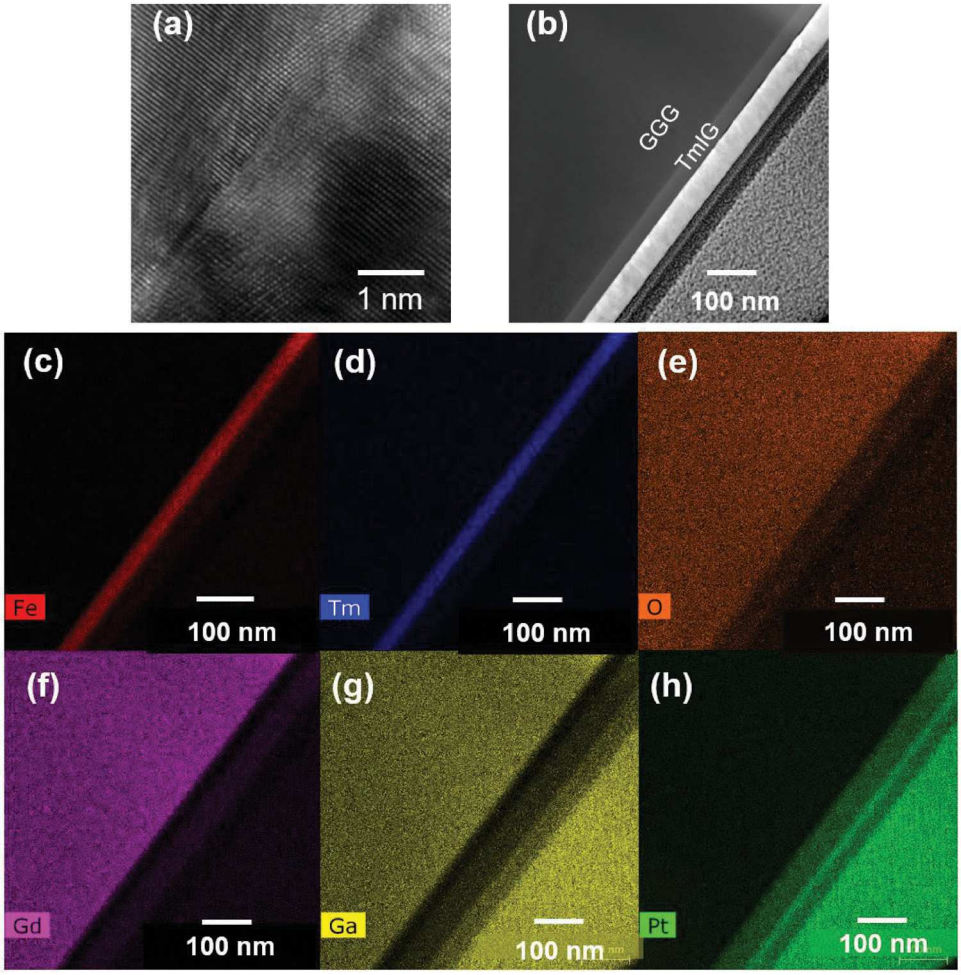

Figure 2. a) HRTEM image of TmIG (32 nm)/GGG substrate, showing periodic lattice, indicative of excellent crystallinity. b) Cross-sectional HAADF-STEM image of the same film. c–h) EDS element maps of Fe, Tm, O, Gd, Ga, and Pt, respectively, separated by different colors.

Longitudinal MOKE (LMOKE) measurement (**Figure** 3a) on TmIG (32 nm)/GGG shows hysteresis loop with a saturation field below 5 mT, while polar MOKE (PMOKE) measurement shows a close to square hysteresis loop (inset of Figure 3a) with a saturation field above 100 mT, indicating approximately in-plane magnetic anisotropy. A nearly opposite behavior is observed on the TmIG films grown on sGGG substrates, i.e., the PMOKE loop shows a saturation magnetic field ≈50 mT with square loop (see Figure 3b) while the LMOKE loop (inset of Figure 3b) shows a saturation field ≈500 mT, an indication of PMA. The high (weak) PMA in TmIG films grown on sGGG (GGG) correlate well with high (low) tensile strain provided by sGGG (GGG), inducing a sizable out-of-plane magnetocrystalline anisotropy in TmIG films.[39] The magnetic anisotropy properties of the TmIG films are further investigated from IP and OOP VSM and FMR measurements. A similar behavior was observed for 12-nm-thick TmIG films grown on both GGG and sGGG substrates and discussed in Section S2 and Figure S2 (Supporting Information). PMOKE measurements on TmIG (7 nm)/GGG are discussed in Section S2 and Figure S5a (Supporting Information).

To further investigate the magnetic properties of the TmIG films, VSM measurements were conducted at room temperature. Figure 3c shows in-plane *M*–*H* hysteresis loops of TmIG (32 nm)/GGG and TmIG (12 nm)/GGG films with a low saturation magnetic field ≈1 mT. OOP *M*–*H* hysteresis loop is plotted in the inset of Figure 3c for TmIG (32 nm)/GGG film with a saturation field ≈100 mT and saturation magnetization M_S of 66 kA m^{-1}. No OOP VSM signal was detected from the TmIG (12 nm)/GGG film due to insufficient sensitivity. The VSM measurements confirm an in-plane easy axis for the TmIG films grown on GGG substrates, consistent with MOKE measurements (discussed above) and previous measurements.[39] Figure 3d displays OOP *M*–*H* hysteresis loops of TmIG (32 nm)/sGGG and TmIG (12 nm)/sGGG films with a saturation magnetic field ≈30 and 10 mT, respectively, and M_S of 70 kA m^{-1}. Inset of Figure 3d depicts IP *M*–*H* loops for TmIG (32 nm)/sGGG and TmIG (12 nm)/sGGG with a saturation magnetic field of 1 and 0.3 T, respectively. The VSM measurements on TmIG/sGGG films confirm out-of-plane easy axis and PMA, consistent with MOKE measurements (discussed above). Temperature-dependent

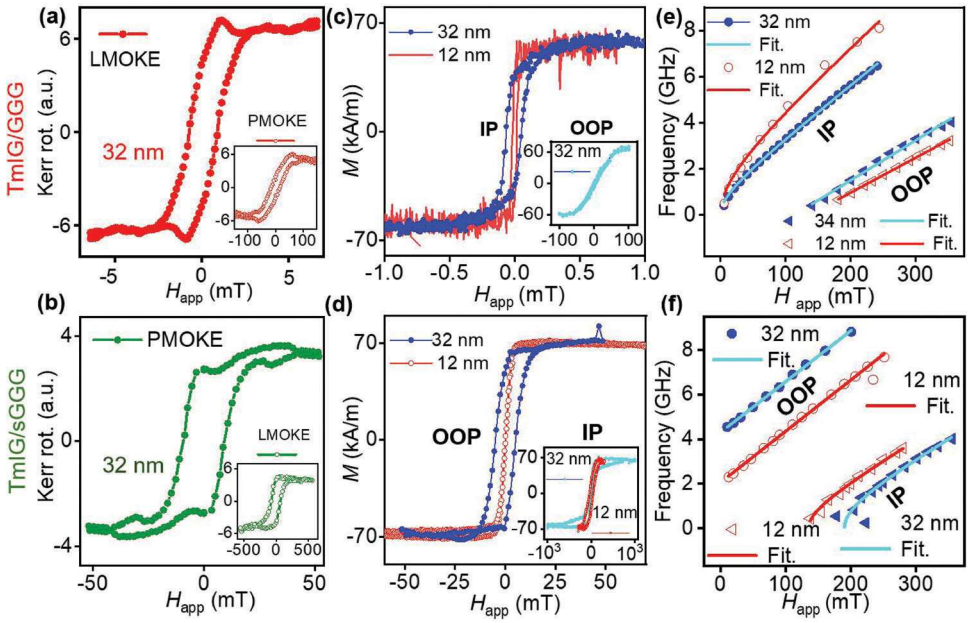

Figure 3. Magnetic characterization of TmIG films. a) LMOKE curve (filled circles) versus applied magnetic field H_{app} of TmIG (32 nm)/GGG. Inset of (a) shows PMOKE (open circles) curve versus H_{app} of TmIG (32 nm)/GGG. b) PMOKE (filled circles) curve versus H_{app} of TmIG (32 nm)/sGGG. Inset of (b) LMOKE curve (open circles) versus H_{app} TmIG (32 nm)/sGGG. c) IP M–H loops of TmIG (32 nm)/GGG (blue filled circles) and TmIG (12 nm)/GGG (red solid line). Inset of (c) OOP loop of TmIG (32 nm)/GGG (sky blue filled circles). d) OOP M–H loops of TmIG (32 nm)/sGGG (blue filled circles) and TmIG (12 nm)/sGGG (red open circles). Inset of (d) IP loop of TmIG (32 nm)/sGGG (sky blue filled circles) and TmIG (12 nm)/sGGG (red open circles). e) FMR IP curves of TmIG (32 nm)/GGG (blue filled circles) and TmIG (12 nm)/GGG (red open circles), and FMR OOP curves of TmIG (32 nm)/GGG (blue filled triangles) and TmIG (12 nm)/GGG (red open triangles), respectively. f) FMR OOP curves of TmIG (32 nm)/sGGG (blue filled circles) and TmIG (12 nm)/sGGG (red open circles), and FMR IP curves of TmIG (32 nm)/sGGG (blue filled triangles) and TmIG (12 nm)/sGGG (red open triangles), respectively. All IP and OOP FMR measured curves are fitted with solid lines.[33]

magnetization measurements (see Figure S3, Supporting Information) on TmIG (32 nm)/GGG and TmIG (32 nm)/sGGG films confirm a Curie temperature > 400 K, mainly limited by the temperature range of our VSM magnetometer, see Section S2 (Supporting Information).

FMR spectroscopy is then used to determine the magnetic properties (magnetic anisotropy and damping) of the TmIG films grown on both GGG and sGGG substrates. A vector network analyzer (Keysight model P5004A) is used to measure the absorption (S_{11} and S_{22} parameters) of the microwave (MW) signal sent through nonmagnetic picoprobes (40A-GSG-150-DP) to coplanar waveguides (CPW) in a ground-signal-ground (GSG) configuration (see **Figure** 4a,b). The CPW were fabricated using direct laser writing (DWL) mask-less optical lithography and subsequent electron-beam deposition of Ti (5 nm)/Au (120 nm). All details of nanofabrication can be found in ref.[33]

Some of the FMR derivative spectra of the TmIG films are discussed in Section S2 and depicted in Figure S4 (Supporting Information) for 12 and 34 nm thick films and Figure S5b (Supporting Information) for 7 nm thick TmIG/GGG film. Figure 3e shows IP and OOP FMR resonance versus H_{app} for TmIG (32 nm)/GGG and TmIG (12 nm)/GGG films. The resonance magnetic field is higher for OOP than IP measurements on TmIG/GGG films for the same FMR frequency, suggesting in-plane magnetic anisotropy. However, TmIG/sGGG films have the opposite behavior, i.e., the resonance magnetic field is higher for IP than OOP measurements, suggesting PMA.[39,40] The IP and OOP measurements in Figure 3e,f were fitted with solid lines.[33,39] leading to gyromagnetic ratio γ of 22.4 GHz T^{-1} and M_S of 66 kA m^{-1} for TmIG (32 nm)/GGG film and γ of 22.87 GHz T^{-1} and M_S of 66 kA m^{-1} for TmIG (12 nm)/GGG film. For the TmIG/sGGG films, the linear fit of the OOP measurements in Figure 3f gives $M_s = 70$ kA m^{-1} (for both 12 and 32 nm films), a negative H_{app}-intercept of −198 and −99 mT for 32 and 12 nm films, respectively. The out-of-plane magnetic anisotropy values are 286 and 187 mT for 32 and 12 nm thick TmIG/sGGG films. The damping constant α varies in the range of 0.0155–0.0365 for IP and OOP FMR measurements done on 32 and 12 nm thick TmIG grown on both GGG and sGGG substrates, consistent with previous FMR measurements.[24,26,33,41] The IP FMR measurements performed on TmIG (7 nm)/GGG film (see Figure S5c, Supporting Information) revealed γ of 22.4 GHz T^{-1}, M_S of 66 kA m^{-1} (82.9 mT), in-plane magnetic anisotropy of 126.8 mT, and α of 0.0122.

2.3. Study of Spin-Wave Propagation Properties in TmIG/GGG Films

To measure the spin-wave transport properties of the TmIG films, SW electrical transmission spectroscopy was performed in the MSSW geometry (Figure 4a), i.e., H_{app} is applied in-plane and perpendicular to the SW propagation wavevector. The spin waves are excited by the MW field, injected through the picoprobe to the CPW antennas (Figure 4b) to measure S_{21} and S_{12} parameters.

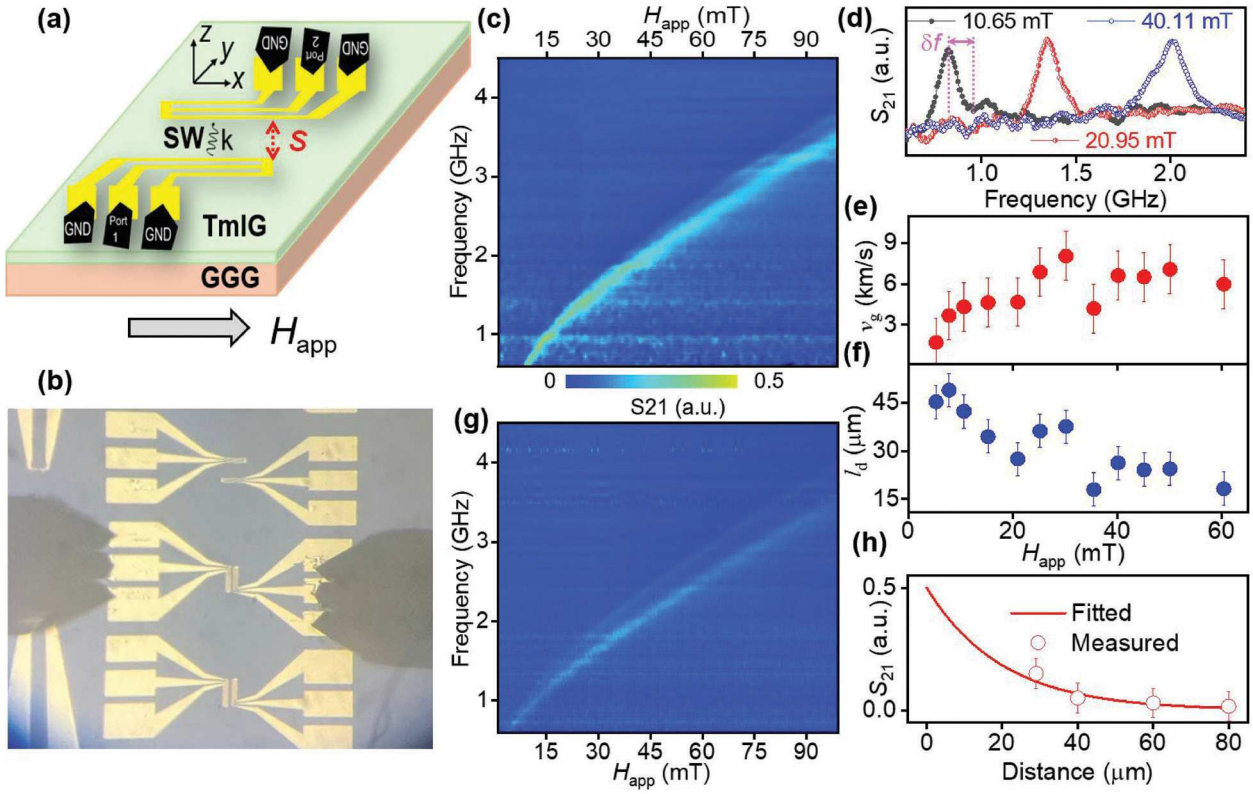

Figure 4. Spin-wave electrical transmission spectroscopy in TmIG (12 nm)/GGG films. a) A schematic of CPWs made on TmIG film. b) A picture of two nonmagnetic picoprobes connected to the GSG CPW antennas. c) SW S_{21} intensity map (MW frequency vs H_{app}) for the MSSW propagation on TmIG (12 nm)/GGG film at a distance S of 32 μm. d) S_{21} intensity versus the MW frequency at H_{app} of 10.65 mT (solid black circles), 20.95 mT (half-filled red circles), and 40.11 mT (open blue circles). e) SW group velocity and f) decay length of MSSWs as function of H_{app}. g) S_{21} intensity map (MW frequency vs H_{app}) of TmIG (12 nm)/GGG at $S = 80$ μm. h) Measured (open red circle) and fitted (red solid line) S_{21} amplitude as function of the distance between MW excitation and SW detection. The solid fit in (h) is an exponential decay function with a decay of 30 μm.

Figure 4c shows the S_{21} intensity map (MW frequency vs H_{app}) of MSSWs measured at a propagation distance S of 32 μm and at a MW power of 1 mW. One dominating SW mode is clearly seen with a wavevector k of 0.2 rad μm^{-1}, given by the GSG geometry of the stripline.[33] Other SW modes with weak amplitude are visible at high magnetic fields (Figure 4c). The frequency of the main SW mode increases with the applied field H_{app} amplitude as expected from the dispersion curve of the MSSWs.[33] In Figure 4d, selected S_{21} spectra are plotted at H_{app} of 10.65, 20.95, and 40.11 mT, respectively. The frequency difference, δf, between two neighboring maxima/minima of the S_{21} parameter gives the SW phase of π, see Figure 4d and Figure S6b in Section S3 (Supporting Information) for further details. The SW group velocity $v_g = \frac{\partial \omega}{\partial k} = \delta f . S$,[32] where S is the separation distance between two CPWs (see Figure 4a). Figure 4e depicts the measured SW group velocity versus the applied magnetic field. v_g is in the range of 3–7 km s^{-1}, slightly higher than the values of 2–4 km s^{-1} obtained from the TmIG (34 nm)/GGG film (see Section S3 and Figure S6, Supporting Information),[33] explained by the narrower spectral S_{21} peaks for the later one. For TmIG (7 nm)/GGG film, v_g is in the range of 2–8 km s^{-1} (see Figure S8, Supporting Information), like the TmIG (12 nm)/GGG film.

The MSSWs decay length is $l_d = \frac{v_g}{2\pi\alpha f}$,[20] where f is the SW resonance frequency and α is the damping constant obtained from FMR measurements (discussed above). l_d is the range of 20–50 μm depending on the amplitude of the applied magnetic field, Figure 4f. This is confirmed from another spectral S_{21} intensity map (MW frequency vs H_{app}) at a distance S of 80 μm, see Figure 4g. The measured SW amplitudes at H_{app} of 20 mT for four distances S of 32, 40, 60, and 80 μm (Figure S7, Supporting Information) are fitted with an exponential decay function (see Figure 4h) with l_d of 30 μm. This value agrees well with the value obtained at H_{app} of 20 mT (see Figure 4f) and are comparable to the values measured on TmIG (32 nm)/GGG films (see Section S3, Supporting Information). It is difficult to extract l_d from TmIG (7 nm)/GGG film due to the very weak and broad SW intensity, see Figure S8 (Supporting Information). The fabrication of smaller (<500 nm) CPW antenna to excite efficiency spin waves and usage of scanning NV magnetometry presents a promising avenue for accurately measuring their decay length and wavelengths.[42,43] SW electrical transmission spectroscopy measurement on TmIG (32 nm)/GGG films (Figure S9, Supporting Information) show FVSWs with l_d up to 32 μm (Section S3, Supporting Information), higher than l_d values (≈0.5 μm) obtained in TmIG (60 nm)/NGG substrates.[31,34]

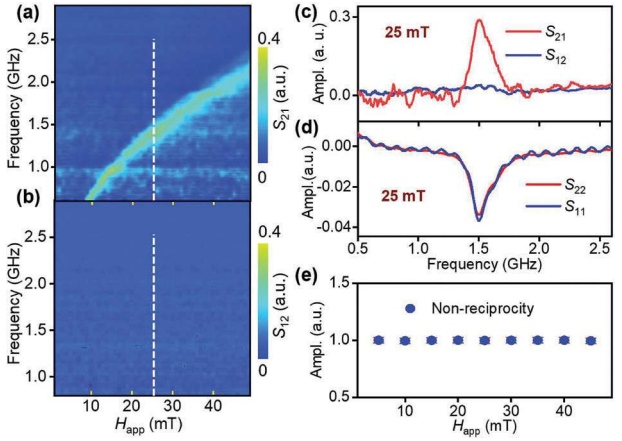

Figure 5. Nonreciprocity properties of MSSWs. a) S_{21} and b) S_{12} intensity maps (MW frequency vs H_{app}) on TmIG (12 nm)/GGG films. c) Line cut plots of S_{21} (red solid line) and S_{12} (blue solid line) at H_{app} of 25 mT. d) Reflection (FMR) parameters S_{11} (blue line) and S_{22} (red line) on TmIG (12 nm)/GGG measured at H_{app} 25 mT. e) Nonreciprocity parameter of MSSWs as a function of H_{app}.

2.4. Spin-Wave Nonreciprocity Properties in TmIG/GGG Films

MSSWs in TmIG/GGG films were also found to exhibit nonreciprocal behavior, confirmed by measuring S_{21} and S_{12} parameters. **Figure** 5a,b shows S_{21} and S_{12} intensity maps (MW frequency vs H_{app}) obtained on TmIG (12 nm)/GGG film at a MW power of 1 mW, respectively. Figure 5c displays the line-cut plots of S_{21} and S_{12} spectra obtained from Figure 5a,b at H_{app} of 25 mT, applied in plane. No SW signal is observed for S_{12} amplitude versus frequency curve, suggesting unidirectional SW propagation. However, S_{11} and S_{22} (reflection) spectra show a similar SW signal (same resonance frequency and amplitude). The nonreciprocity parameter β from SW transmission spectra is defined as.[20] $\beta = \frac{S_{21}}{S_{12}+S_{21}}$. Figure 5e shows β of 1 as function of H_{app} in the range of 5–45 mT, implying a strong nonreciprocal behavior of MSSWs.[16]

The nonreciprocal property is observed when the excited spin waves by the CPW antenna produce stray magnetic fields along y (H_y) and z (H_z) directions with amplitudes larger in phase compared to the out-of-phase.[44] A similar behavior is observed for TmIG (32 nm)/GGG films (see Figure S10, Supporting Information). Prior measurements have shown nonreciprocal propagation of spin waves in YIG (100 nm)/GGG[16,45] and permalloy (20 nm) film.[46] This is the first experimental measurement of SW nonreciprocity on TmIG/GGG films, expanding its applications in miniaturized, broad band, and highly tunable isolators within microwave circuits for spin wave computing, a field where magnons serve as carriers, transporters, and processors of information.[16]

2.5. Study of Forward Volume Spin-Wave Properties in TmIG/sGGG Films

TmIG films grown on sGGG substrates have PMA (discussed above), and no SW transmission is observed in plane (i.e., MSSW geometry). **Figure** 6a,b shows the SW S_{21} and S_{12} intensity maps (MW frequency vs H_{app}) of TmIG (32 nm)/sGGG, respectively, measured in FVSW geometry (i.e., magnetic field is applied perpendicular to the sample plane) at a propagation distance S of 32 µm and MW power of 1 mW. The amplitude of the measured FVSW (see Figure 6c at H_{app} of 142 mT) is weak in comparison to the MSSW measured on TmIG (12–34 nm)/GGG films (Figures S6 and S7, Supporting Information). This can be explained by the large separation distance (3.5 µm) between the CPW antenna, compared to the short wavelength (<500 nm) of the FVSWs, resulting in inefficient MW excitation.[14] Indeed, the S_{21} parameter shows similar resonance and amplitude to S_{12} at 142 mT suggesting a bidirectional propagation of FVSWs. Similar strength and amplitude of S_{11} and S_{22} reflection spectra at 142 mT (see Figure 6d), suggests the proper functioning of our CPW antennas. This marks the first experimental measurements of FVSWs in TmIG/sGGG with PMA. Figure 6e shows almost perfect reciprocal behavior ($\beta = 0.5$) of the FVSWs over a wide range of applied magnetic fields.

3. Conclusions

In summary, spin-wave propagation properties are studied in epitaxially grown TmIG films on GGG and sGGG substrates. Magnetic measurements via MOKE, FMR, and VSM confirm in-plane easy axis for TmIG grown on GGG and an out-of-plane easy axis for TmIG grown on sGGG. SW transmission electrical spectroscopy show propagating MSSWs in TmIG/GGG films up to ≈80 µm and SW velocity of 2–8 km s^{-1}, depending on the strength of the applied magnetic field. The extended decay lengths signify enhanced SW transport efficiency, offering promising avenues for the development of low loss magnonic devices. Notably, our experimental results reveal nonreciprocal propagation of MSSWs in TmIG/GGG films, suggesting

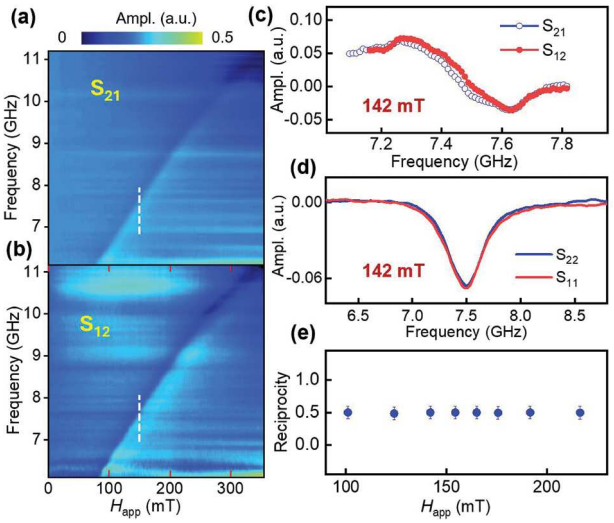

Figure 6. a) S_{21} and b) S_{12} intensity maps (MW frequency vs H_{app}) for FVSWs propagation on TmIG (32 nm)/sGGG at a separation distance S of 32 µm. c) Line cuts of S_{21} (blue open circles) and S_{12} (filled red circles) at 142 mT, extracted from (a) and (b), highlighted by dashed lines. d) S_{11} (red solid line) and S_{22} (blue solid line) of TmIG (32 nm)/sGGG measured at 142 mT. e) Reciprocity parameter versus H_{app} of FVSWs.

potential applications in nonreciprocal magnonics and logic devices.[45] TmIG films grown on sGGG exhibit isotropic propagation of FVSWs with a long SW decay length of 32 µm.

TmIG has the potential to host topological spin textures,[29] paving the way for investigating new magnetic phenomena such as the interaction between skyrmions and spin waves[47] or topological magnons.[48] The usage of scanning NV magnetometry[43,49,50] may allow mapping of spin waves in TmIG with a short wavelength (<100 nm), opening new avenues for using spin waves in magnetic insulators in magnon spintronics,[13] and as quantum buses for applications in quantum information processing.[51–53]

Supporting Information

Supporting Information is available from the Wiley Online Library or from the author.

Acknowledgements

This material is based upon work supported by the NSF/EPSCoR RII Track-1: Emergent Quantum Materials and Technologies (EQUATE) Award OIA-2044049 and NSF Award No. 2328822. The research was performed in part in the Nebraska Nanoscale Facility: National Nanotechnology Coordinated Infrastructure and the Nebraska Center for Materials and Nanoscience (and/or NERCF), which were supported by NSF under Award ECCS: 2025298, and the Nebraska Research Initiative.

Conflict of Interest

The authors declare no conflict of interest.

Author Contributions

R.T. performed FMR and SW electrical transmission spectroscopy on TmIG films; H.W. grew the TmIG films; B.G. performed MOKE measurements; A.E. assisted R.T. in AFM measurements; S.S. and J.E.S. performed HRTEM, STEM, and EDS measurements; S.L. and S.-Y.L. performed XPS spectroscopy; X.X. and A.L. designed the experiments and supervised the project; R.T. wrote the manuscript with assistance from A.L. and contributions of all authors.

Data Availability Statement

The data that support the findings of this study are available from the corresponding author upon reasonable request.

Keywords

ferromagnetic resonance, nonreciprocity, rare-earth garnet, spin waves, thulium iron garnet

Received: May 16, 2024
Revised: July 11, 2024
Published online:

[1] T. Sebastian, K. Schultheiss, B. Obry, B. Hillebrands, H. Schultheiss, *Front. Phys.* **2015**, *3*, 1.
[2] H. Schultheiss, X. Janssens, M. van Kampen, F. Ciubotaru, S. J. Hermsdoerfer, B. Obry, A. Laraoui, A. A. Serga, L. Lagae, A. N. Slavin, B. Leven, B. Hillebrands, *Phys. Rev. Lett.* **2009**, *103*, 157202.
[3] L. Berger, *Phys. Rev. B.* **1996**, *54*, 9353.
[4] M. Collet, X. de Milly, O. d'Allivy Kelly, V. V. Naletov, R. Bernard, P. Bortolotti, J. Ben Youssef, V. E. Demidov, S. O. Demokritov, J. L. Prieto, M. Muñoz, V. Cros, A. Anane, G. de Loubens, O. Klein, *Nat. Commun.* **2016**, *7*, 10377.
[5] P. Andrich, C. F. de las Casas, X. Liu, H. L. Bretscher, J. R. Berman, F. J. Heremans, P. F. Nealey, D. D. Awschalom, *npj Quantum Inf.* **2017**, *3*, 28.
[6] I. Bertelli, J. J. Carmiggelt, T. Yu, B. G. Simon, C. C. Pothoven, G. E. W. Bauer, Y. M. Blanter, J. Aarts, T. Van Der Sar, *Sci. Adv.* **2020**, *6*, eabd3556.
[7] T. An, V. I. Vasyuchka, K. Uchida, A. V. Chumak, K. Yamaguchi, K. Harii, J. Ohe, M. B. Jungfleisch, Y. Kajiwara, H. Adachi, B. Hillebrands, S. Maekawa, E. Saitoh, *Nat. Mater.* **2013**, *12*, 549.
[8] A. Laraoui, V. Halté, M. Vomir, J. Vénuat, M. Albrecht, E. Beaurepaire, J.-Y. Bigot, *Eur. Phys. J. D.* **2007**, *43*, 251.
[9] M. Vomir, L. H. F. Andrade, L. Guidoni, E. Beaurepaire, J.-Y. Bigot, *Phys. Rev. Lett.* **2005**, *94*, 237601.
[10] J. R. Hortensius, D. Afanasiev, M. Matthiesen, R. Leenders, R. Citro, A. V. Kimel, R. V. Mikhaylovskiy, B. A. Ivanov, A. D. Caviglia, *Nat. Phys.* **2021**, *17*, 1001.
[11] D. Kikuchi, D. Prananto, K. Hayashi, A. Laraoui, N. Mizuochi, M. Hatano, E. Saitoh, Y. Kim, C. A. Meriles, T. An, *Appl. Phys. Express* **2017**, *10*, 103004.
[12] K. An, V. S. Bhat, M. Mruczkiewicz, C. Dubs, D. Grundler, *Phys. Rev. Appl.* **2019**, *11*, 034065.
[13] A. V. Chumak, V. I. Vasyuchka, A. A. Serga, B. Hillebrands, *Nat. Phys.* **2015**, *11*, 453.
[14] J. Solano, O. Gladii, P. Kuntz, Y. Henry, D. Halley, M. Bailleul, *Phys. Rev. Mater.* **2022**, *6*, 124409.
[15] C. Liu, J. Chen, T. Liu, F. Heimbach, H. Yu, Y. Xiao, J. Hu, M. Liu, H. Chang, T. Stueckler, S. Tu, Y. Zhang, Y. Zhang, P. Gao, Z. Liao, D. Yu, K. Xia, N. Lei, W. Zhao, M. Wu, *Nat. Commun.* **2018**, *9*, 738.
[16] Y. Li, T.-H. Lo, J. Lim, J. E. Pearson, R. Divan, W. Zhang, U. Welp, W.-K. Kwok, A. Hoffmann, V. Novosad, *Appl. Phys. Lett.* **2023**, *123*, 022406.
[17] V. E. Demidov, S. O. Demokritov, K. Rott, P. Krzysteczko, G. Reiss, *J. Phys. Appl. Phys.* **2008**, *41*, 164012.
[18] A. B. Ustinov, B. A. Kalinikos, E. Lähderanta, *J. Appl. Phys.* **2013**, *113*, 113904.
[19] L. Zheng, L. Jin, T. Wen, Y. Liao, X. Tang, H. Zhang, Z. Zhong, *J. Phys. Appl. Phys.* **2022**, *55*, 263002.
[20] F. Ciubotaru, T. Devolder, M. Manfrini, C. Adelmann, I. P. Radu, *Appl. Phys. Lett.* **2016**, *109*, 012403.
[21] B. W. Zingsem, M. Winklhofer, R. Meckenstock, M. Farle, *Phys. Rev. B* **2017**, *96*, 224407.
[22] G. Varvaro, S. Laureti, D. Fiorani, *J. Magn. Magn. Mater.* **2014**, *368*, 415.
[23] L. Alahmed, P. Li, in *Magnetic Materials and Magnetic Levitation*, (Eds.: D. R. Sahu, V. N. Stavrou), IntechOpen, London, UK **2021**.
[24] O. Ciubotariu, A. Semisalova, K. Lenz, M. Albrecht, *Sci. Rep.* **2019**, *9*, 17474.
[25] A. Quindeau, C. O. Avci, W. Liu, C. Sun, M. Mann, A. S. Tang, M. C. Onbasli, D. Bono, P. M. Voyles, Y. Xu, J. Robinson, G. S. D. Beach, C. A. Ross, *Adv. Electron. Mater.* **2017**, *3*, 1600376.
[26] C. N. Wu, C. C. Tseng, Y. T. Fanchiang, C. K. Cheng, K. Y. Lin, S. L. Yeh, S. R. Yang, C. T. Wu, T. Liu, M. Wu, M. Hong, J. Kwo, *Sci. Rep.* **2018**, *8*, 11087.
[27] L. Caretta, E. Rosenberg, F. Büttner, T. Fakhrul, P. Gargiani, M. Valvidares, Z. Chen, P. Reddy, D. A. Muller, C. A. Ross, G. S. D. Beach, *Nat. Commun.* **2020**, *11*, 1090.

[28] C. O. Avci, E. Rosenberg, L. Caretta, F. Büttner, M. Mann, C. Marcus, D. Bono, C. A. Ross, G. S. D. Beach, *Nat. Nanotechnol.* **2019**, *14*, 561.
[29] A. S. Ahmed, A. J. Lee, N. Bagués, B. A. McCullian, A. M. A. Thabt, A. Perrine, P.-K. Wu, J. R. Rowland, M. Randeria, P. C. Hammel, D. W. McComb, F. Yang, *Nano Lett.* **2019**, *19*, 5683.
[30] Q. Shao, C. Tang, G. Yu, A. Navabi, H. Wu, C. He, J. Li, P. Upadhyaya, P. Zhang, S. A. Razavi, Q. L. He, Y. Liu, P. Yang, S. K. Kim, C. Zheng, Y. Liu, L. Pan, R. K. Lake, X. Han, Y. Tserkovnyak, J. Shi, K. L. Wang, *Nat. Commun.* **2018**, *9*, 3612.
[31] L. Sheng, Y. Liu, J. Chen, H. Wang, J. Zhang, M. Chen, J. Ma, C. Liu, S. Tu, C.-W. Nan, H. Yu, *Appl. Phys. Lett.* **2020**, *117*, 232407.
[32] J. Xu, D. Zhang, Y. Zhang, Z. Zhong, H. Zhang, X. Xu, X. Luo, Q. Yang, B. Liu, L. Jin, *AIP Adv.* **2022**, *12*, 065026.
[33] R. Timalsina, H. Wang, B. Giri, A. Erickson, X. Xu, A. Laraoui, *Adv. Electron. Mater.* **2024**, *10*, 2300648.
[34] J. Čermák, A. Abrahám, T. Fabián, P. Kaboš, P. Hyben, *J. Magn. Magn. Mater.* **1990**, *83*, 427.
[35] N. S. Rajput, K. Sloyan, D. H. Anjum, M. Chiesa, A. A. Ghaferi, *Ultramicroscopy* **2022**, *235*, 113496.
[36] G. Greczynski, L. Hultman, *J. Appl. Phys.* **2022**, *132*, 011101.
[37] S. Lamichhane, R. Timalsina, C. Schultz, I. Fescenko, K. Ambal, S.-H. Liou, R. Y. Lai, A. Laraoui, *Nano Lett* **2024**, *24*, 873.
[38] R. Sharma, P. K. Ojha, S. Choudhary, S. K. Mishra, *Mater. Lett.* **2023**, *352*, 135154.
[39] A. J. Lee, A. S. Ahmed, B. A. McCullian, S. Guo, M. Zhu, S. Yu, P. M. Woodward, J. Hwang, P. C. Hammel, F. Yang, *Phys. Rev. Lett.* **2020**, *124*, 257202.
[40] C. Tang, P. Sellappan, Y. Liu, Y. Xu, J. E. Garay, J. Shi, *Phys. Rev. B.* **2016**, *94*, 140403.
[41] S. Crossley, A. Quindeau, A. G. Swartz, E. R. Rosenberg, L. Beran, C. O. Avci, Y. Hikita, C. A. Ross, H. Y. Hwang, *Appl. Phys. Lett.* **2019**, *115*, 172402.
[42] A. Erickson, S. Q. Abbas Shah, A. Mahmood, I. Fescenko, R. Timalsina, C. Binek, A. Laraoui, *RSC Adv.* **2023**, *13*, 178.
[43] B. G. Simon, S. Kurdi, J. J. Carmiggelt, M. Borst, A. J. Katan, T. van der Sar, *Nano Lett.* **2022**, *22*, 9198.
[44] S. Klingler, P. Pirro, T. Brächer, B. Leven, B. Hillebrands, A. V. Chumak, *Appl. Phys. Lett.* **2015**, *106*, 212406.
[45] J. Chen, H. Yu, G. Gubbiotti, *J. Phys. Appl. Phys.* **2022**, *55*, 123001.
[46] M. Jamali, J. H. Kwon, S.-M. Seo, K.-J. Lee, H. Yang, *Sci. Rep.* **2013**, *3*, 3160.
[47] N. Tang, W. L. N. C. Liyanage, S. A. Montoya, S. Patel, L. J. Quigley, A. J. Grutter, M. R. Fitzsimmons, S. Sinha, J. A. Borchers, E. E. Fullerton, L. DeBeer-Schmitt, D. A. Gilbert, *Adv. Mater.* **2023**, *35*, 2300416.
[48] P. A. McClarty, *Annu. Rev. Condens. Matter Phys.* **2022**, *13*, 171.
[49] A. Laraoui, K. Ambal, *Appl. Phys. Lett.* **2022**, *121*, 060502.
[50] T. X. Zhou, J. J. Carmiggelt, L. M. Gächter, I. Esterlis, D. Sels, R. J. Stöhr, C. Du, D. Fernandez, J. F. Rodriguez-Nieva, F. Büttner, E. Demler, A. Yacoby, *Proc. Natl. Acad. Sci. USA* **2021**, *118*, 2019473118.
[51] D. D. Awschalom, C. R. Du, R. He, F. J. Heremans, A. Hoffmann, J. Hou, H. Kurebayashi, Y. Li, L. Liu, V. Novosad, J. Sklenar, S. E. Sullivan, D. Sun, H. Tang, V. Tyberkevych, C. Trevillian, A. W. Tsen, L. R. Weiss, W. Zhang, X. Zhang, L. Zhao, C.h. W. Zollitsch, *IEEE Trans. Quantum Eng.* **2021**, *2*, 5500836.
[52] D. Xu, X.-K. Gu, H.-K. Li, Y.-C. Weng, Y.-P. Wang, J. Li, H. Wang, S.-Y. Zhu, J. Q. You, *Phys. Rev. Lett.* **2023**, *130*, 193603.
[53] M. Fukami, D. R. Candido, D. D. Awschalom, M. E. Flatté, *PRX Quantum* **2021**, *2*, 040314.